Revisiting two thiophosphate compounds constituting d^0 transition metal: HfP_2S_6 and d^{10} transition metal: α-$Ag_4P_2S_6$ as multifunctional materials for combining second harmonic

Journal:	*CrystEngComm*
Manuscript ID	CE-ART-11-2022-001576.R1
Article Type:	Paper
Date Submitted by the Author:	02-Jan-2023
Complete List of Authors:	Cropek, Craig; Wichita State University Ji, Bingheng; Wichita State University, Department of Chemistry and Biochemistry Sarkar, Arka; Iowa State University, Department of Chemistry and Biochemistry Wang, Fei; Missouri State University Syed, Tajamul Hussain; Wichita State University Wei, Wei; Wichita State University, Mechanical Engineering Guo, Sheng-Ping; Yangzhou University, School of Chemistry and Chemical Engineering Wang, Jian; Wichita State University, Chemistry

Revisiting two thiophosphate compounds constituting d^0 transition metal: HfP_2S_6 and d^{10} transition metal: α-$Ag_4P_2S_6$ as multifunctional materials for combining second harmonic generation response and photocurrent response

Craig Cropek [a, #], Bingheng Ji [a, #], Arka Sarkar [b], Fei Wang [c], Tajamul Hussain Syed [d], Wei Wei [d], Sheng-Ping Guo [e], Jian Wang [a] *

[a] *Department of Chemistry and Biochemistry, Wichita State University, Wichita, Kansas 67260, United States*

[b] *Department of Chemistry, Iowa State University, Ames, Iowa, 50011, United States*

[c] *Department of Chemistry, Missouri State University, Springfield, Missouri, 65897, United States*

[d] *Department of Mechanical Engineering, Wichita State University, Wichita, Kansas 67260, United States*

[e] *School of Chemistry and Chemical Engineering, Yangzhou University, Yangzhou, Jiangsu 225002, P. R. China*

[#] equally contributed.

Abstract:

Two acentric thiophosphate compounds, HfP_2S_6 and α-$Ag_4P_2S_6$, are revisited and studied as infrared nonlinear optical materials. HfP_2S_6 and α-$Ag_4P_2S_6$ were structurally characterized without any property measurements. In this work, HfP_2S_6 and α-$Ag_4P_2S_6$ were synthesized via high temperature salt flux reactions. Low-temperature polymorph acentric α-$Ag_4P_2S_6$ was purified and grown as mm-sized crystals with the aid of AgBr flux. The AgBr flux was revealed to play an important role in stabilizing the acentric α-$Ag_4P_2S_6$. The acentric α-$Ag_4P_2S_6$ transfers to centrosymmetric β- $Ag_4P_2S_6$ at 850(5) K, which is revealed by differential scanning calorimetry (DSC) analysis and powder X-ray diffraction experiments. HfP_2S_6 and α-$Ag_4P_2S_6$ are discovered by UV-Vis spectrum measurements as indirect bandgap semiconductors with bandgaps of 2.2(1) eV and 2.5(1) eV, respectively, which is supported by DFT calculations and TB-LMTO-ASA calculations. The bonding pictures of α-$Ag_4P_2S_6$ were studied by crystal orbital Hamilton populations calculations (COHP) coupled with electron localization function (ELF) analysis. DFT calculations predicts that HfP_2S_6 and α-$Ag_4P_2S_6$ would exhibit different optical performance regardless of being constructed by identical [P_2S_6] motifs. HfP_2S_6 exhibits a low second harmonic generation (SHG) response, ~0.21×AGS (for the sample of particle size of 25 μm). α-$Ag_4P_2S_6$ possesses moderate SHG response, ~0.61×AGS (for the sample of particle size of 225 μm) coupled with a high laser damage threshold (LDT) of ~3.2×AGS. Characteristics of high ambient stability, moderate bandgap and SHG response, type-I phase-matching capability, and high LDT together with the easy growth of large crystals makes α-$Ag_4P_2S_6$ attractive for future infrared nonlinear optical applications. Photocurrent measurements found that α-$Ag_4P_2S_6$ and β-$Ag_4P_2S_6$ have high photocurrent response, 165 nA cm^{-2} and 135 nA cm^{-2}, respectively. α-$Ag_4P_2S_6$ is a new multifunctional material of the ternary Ag-P-S system, which combines nonlinear optical (NLO) properties and photocurrent response.

Introduction

Infrared nonlinear optical materials have sparked continual research interests due to their critical role of the process of second harmonic generation process, which is employed to expand the wavelength of infrared lasers. Due to their important applications, infrared nonlinear optical materials are heavily studied. After many years of intensive study, few materials, including $AgGaS_2$, $ZnGeP_2$, and $AgGaSe_2$, have been commercialized due to their balanced properties which play an important role in scientific research and industrial applications [1-29]. These commercial materials, $AgGaS_2$, $ZnGeP_2$, and $AgGaSe_2$, are impeded from high energy use due to their intrinsic limitations including low laser damage threshold, double-photon absorption, and non-phase-matching behavior, respectively[13, 30-32]. In addition to energy loss, these commercial materials cannot be employed to cover the full range of the infrared spectrum. Hence, uncovering new infrared nonlinear optical materials are extremely important.

Thiophosphates, which combines both phosphorus and sulfur, are demonstrated to be good candidates for infrared nonlinear optical materials, where the promising properties originate from structure and chemical flexibility. The flexible [P_xS_y] motifs interact with various cations generate many promising nonlinear optical materials including $Rb_2Ga_2P_2S_9$ [33], [K_3Cl][Ga_3PS_8] [34], [Rb_3Cl][Ga_3PS_8] [34], [K_3Br][Ga_3PS_8] [34], [Rb_3Br][Ga_3PS_8] [34], $LiZnPS_4$ [35], $CuZnPS_4$ [36], $CuHgPS_4$ [37], $AgZnPS_4$ [35], Ag_3PS_4 [38], $LiGa_2PS_6$ [39], $AgGa_2PS_6$ [40], $LiCd_3PS_6$ [39], $CuCd_3PS_6$ [41], $AgCd_3PS_6$ [42], $Zn_3P_2S_8$ [43], $Hg_3P_2S_8$ [44], $Sn_2P_2S_6$ [45-47], $KBiP_2S_6$ [48], $K_2BaP_2S_6$ [49], $KSbP_2S_6$ [49], $Pb_2P_2S_6$ [50], α-$Ba_2P_2S_6$ [50], $Pb_3P_2S_8$ [51], $RbBiP_2S_6$ [52], $Eu_2P_2S_6$ [53], $Hg_2P_2S_6$ [54], $ASrPS_4$ (A = Li, Na, K, Rb, Cs) [55], AAg_2PS_4 (A = K, Na/K) [56], etc. From the perspective of the constituting cations, the most explored cations for thiophosphate nonlinear optical materials are alkali metals and d^{10} transition metals. The d^0 transition metals, which contribute to the Jahn-Tell distortion and lack *d-d* transition are important building elements for nonlinear optical materials. In this work, we present the synthesis and linear and nonlinear optical properties of the first d^0 transition metal constituting NLO thiophosphate material, HfP_2S_6. Another known d^{10} transition metal constituting NLO material, α-$Ag_4P_2S_6$, is also discussed in this work and is constructed by identical [P_2S_6] motifs as HfP_2S_6. The polymorphism of $Ag_4P_2S_6$ is discussed in this work. AgBr was employed to stabilize the acentric α-$Ag_4P_2S_6$. The structure, crystal growth, electronic structure, bonding picture studies and NLO properties of HfP_2S_6 and α-$Ag_4P_2S_6$ are discussed in this work. α-$Ag_4P_2S_6$ and β-$Ag_4P_2S_6$ were also found to show promising photocurrent response.

Experimental Procedures

Synthesis. All starting materials were stored in an argon-filed glovebox with oxygen levels below 0.5 ppm. All starting materials were commercial grade and used without any further purifications: Hf powder (Alfa Aesar, 99.6%), Ag powder (Fisher Scientific, 99.9%), P powder (Alfa Aesar. 99.5%), S powder (Alfa Aesar, 99.5%), $AlCl_3$ (Alfa Aesar, 99.99%), KCl (Sigma Aldrich, 99+%), NaCl (Sigma Aldrich, 99+%), AgBr (Thermo scientific, 99.5%).

HfP_2S_6: HfS_2 was made as a precursor of HfP_2S_6 first by mixing stoichiometric amounts of Hf and S powder into a flame-sealed silica tube under vacuum. Next, the tube was heated at 1073K for 24 hours and naturally cooled down to room temperature by turning off the furnace. Orange-red powder was produced with a small weight loss of less than 10%. After precursor was made, HfS_2: P: S = 1: 2: 4 was loaded into a silica tube, with addition of $AlCl_3$/KCl/NaCl (AKN) as a flux and the molar ratio of $AlCl_3$: KCl: NaCl = 0.601:0.141:0.258, under an argon-filled environment. The flux/reactants mass ratio is 1:1. A total of 0.8 g of materials, including reactants plus flux, were added to silica ampoules. The silica ampoules were flame-sealed under vacuum and placed in a conventional furnace. The furnace was set to heat up to 973K in 20 hours and kept for 96 hours. Next, the furnace cooled down to 573K and eventually dwelled there for about 10 hours. The tube was centrifuged to remove AKN flux, and a resulting plum colored polycrystalline material was collected. HfP_2S_6 is stable in air for many months.

α-$Ag_4P_2S_6$: 0.4 g of elemental reactants were loaded into carbonized silica ampoules at a molar ratio of Ag:P:S = 4:2:6. A mass of silver bromide, equivalent to the sum of all the elements, was added as flux. The reactants and flux were sealed into a 9 mm inner diameter carbonized quartz tube which contained quartz wool, over said reactants, and broken pieces of quartz above the quartz wool. The ampoules were heated to a temperature of 1073K in 20 hours, dwelled at 1073 K for

120 hours, ramped down to 723 K in 24 hours, and then dwelled for a max of 48 hours, or until removed. Flux was removed via centrifugation during the final dwell step around 24 hours of dwell time. Yellow-needle crystals of α-$Ag_4P_2S_6$ were collected after opening the ampoules (*vide infra*). α-$Ag_4P_2S_6$ is stable in air for several months.

β-$Ag_4P_2S_6$: 0.4 g of elemental reactants were loaded into carbonized silica ampoules at a molar ratio of Ag:P:S = 4:2:6. The reactants were sealed under vacuum and heated to 1073 K for 20 hours and held at 1073 K for 120 hours, then slowly cool down to room temperature.

Lab powder X-ray Diffraction and 11BM data. Powder X-ray diffraction data were collected at room temperature using a Rigaku Mini Flex 6S diffractometer with Cu-Kα radiation (λ =1.5406 Å) in the range 2θ = 10° – 80°, at a scan step of 0.04° with ten seconds exposure time. High-resolution room temperature synchrotron X-ray diffraction data of α-$Ag_4P_2S_6$ were collected at beamline 11-BM (calibrated wavelength λ = 0. 458935 Å) at the Advanced Photon Source (APS) at Argonne National Laboratory (ANL). There were two polymorphs of $Ag_4P_2S_6$ reported. The high-resolution synchrotron X-ray diffraction was employed to verify the purity of acentric α-$Ag_4P_2S_6$ (*vide infra*). The purity of α-$Ag_4P_2S_6$ was verified as single-phase samples by both lab powder X-ray diffraction measurements and synchrotron X-ray powder diffraction results (*vide infra*).

UV-Vis Measurements and IR spectroscopy. Diffuse-reflectance spectra were recorded at room temperature by a PERSEE-T8DCS UV-Vis spectrophotometer equipped with an integrating sphere in the wavelength range of 230−850 nm. The reflectance data, R, were recorded and converted to the Kubelka-Munk function, $f(R)=(1-R)^2(2R)^{-1}$. The Tauc plots, $(KM*E)^2$ and $(KM*E)^{1/2}$, were applied to estimate direct and indirect bandgaps, respectively. IR Spectroscopy:

The IR spectra were recorded using an AVATAR 360 70 FT–IR spectrophotometer in the range of 4000–400 cm^{-1} on powder samples.

Second Harmonic Measurements. Using the Kurtz and Perry method,[57] powder SHG responses of HfP_2S_6 and α-$Ag_4P_2S_6$ compounds were investigated by a Q-switch laser (2.09 μm, 3 Hz, 50 ns) with various particle sizes, including 38.5–54, 54–88, 88–105, 105–150, and 150–200 μm. Homemade $AgGaS_2$ was selected as the reference. The lab-synthesized $AgGaS_2$ crystals were ground to the same size range as HfP_2S_6 and α-$Ag_4P_2S_6$. The LDTs of the title compounds were evaluated on powder samples (150−200 μm) with a pulsed YAG laser (1.06 μm, 10 ns, 10 Hz). The judgment criterion are as follows: with increasing laser energy, the color change of the powder sample is constantly observed by an optical microscope to determine the damage threshold. To adjust different laser beams, an optical concave lens is added to the laser path. The damaged spot is measured by the scale of the optical microscope.

DFT Calculations. To study their electronic structures, the density of states (DOS) curves and band structures of HfP_2S_6 and α-$Ag_4P_2S_6$ were calculated with first-principle DFT calculations using Vienna Ab Initio Software Package (VASP) [58-61]. Pseudopotentials generated with the projector augmented-wave (PAW) method [62] were employed. The Perdew-Burke-Ernzerhof (PBE) generalized gradient approximation [63] was employed to treat the electronic exchange-correlation. A 5 × 5 × 9 (HfP_2S_6) and 7 × 5 × 3 (α-$Ag_4P_2S_6$) Monkhorst mesh [64] was used to sample the first Brillouin zones. The energy cutoff of the plane wave basis set is 258.7 eV for both HfP_2S_6 and α-$Ag_4P_2S_6$. The band structures were calculated along paths connecting the special points in the first Brillouin zones defined by Setyawan and Curtarolo [65]. Birefringence calculations: The birefringence values of HfP_2S_6 and α-$Ag_4P_2S_6$ were calculated based on ab initio calculations implemented in the CASTEP package through density functional theory (DFT) [66]. The Heyd-Scuseria-Ernzerhof hybrid functional (HSE) function [67,68] was adopted to calculate the exchange-correlation potential, with an energy cutoff of 720 eV and 850 eV for HfP_2S_6 and α-

$Ag_4P_2S_6$, respectively. The numerical integration of the Brillouin zone was performed using Monkhorst–Pack 2 × 3 × 1 and 2 × 2 × 4 *k*-point meshes for HfP_2S_6 and α-$Ag_4P_2S_6$, respectively.

TB-LMTO-ASA calculations. The density of states (DOS), partial density of states (PDOS), band structure, crystal orbital Hamilton population (COHP), and electron localization function (ELF) of α-$Ag_4P_2S_6$ were calculated using the tight binding-linear muffin tin orbitals-atomic sphere approximation (TB-LMTO-ASA) program [69]. The Barth-Hedin exchange potential was employed for the LDA calculations [70]. The radial scalar-relativistic Dirac equation was solved to obtain the partial waves. The basis set used contained Ag (*5s, 5p,* 4*d, 4f*), P (3s, 3p) and S (3*s*, 3*p*) orbitals, and was employed for a self-consistent calculation, with downfolded functions of Ag (*4f*), P (*3d*) and S (3*d*). The density of states and band structures were calculated after converging the total energy on a dense k-mesh of α-$Ag_4P_2S_6$ (12×12×24 points with 912 irreducible k-points).

Photocurrent response measurement. Crystals of α-$Ag_4P_2S_6$ and β-$Ag_4P_2S_6$ were manually grounded into fine power with the aid of ethanol. The fine powders of α-$Ag_4P_2S_6$ and β-$Ag_4P_2S_6$ were mixed with ethanol to form a suspension solution. The suspension solution was dropped to the ITO glass to form a uniform film. The uniformness of the prepared films was checked by an optical microscope. The films were dried at 393K under vacuum for 3 hours. The photocurrent performance of the photoanode was evaluated in a conventional three-electrode configuration, consisting of α-$Ag_4P_2S_6$ or β-$Ag_4P_2S_6$ photoanode as the working electrode, platinum wire as the counter electrode, and Ag/AgCl as the reference electrode. 1M Na_2SO_4 aqueous solution was used as the electrolyte. Linear sweep voltammetry and I-t scans were collected on the electrochemical workstation (Gamry Interface 5000) under illumination of AM 1.5 (1 sun, 100 mW/cm^2) using a solar simulator (Newport).

Results and Discussion

Synthesis of HfP_2S_6.

HfP_2S_6 was discovered by Simon, A. et al. in 1985 [71]. Our attempt to obtain a single phase of HfP_2S_6 failed. Many experiments were tried. Elemental reactants were tried first by heating from 973K to 1373K, which resulted in HfP_2S_6 mixed with a significant amount of HfS_2. Since HfS_2 has a very stable nature, HfS_2 was employed as a precursor. The mixing of HfS_2/P/S in different ratios also failed to increase the yield of HfP_2S_6. Then we moved to salt flux method. Employing AKN flux plus centrifuging to remove AKN flux proved to be the best method, which generated a significant amount of HfP_2S_6. There were small amounts of HfS_2 present in HfP_2S_6 sample as shown in **Figure S1**. Due to the centrosymmetric nature of HfS_2, the contribution of HfS_2 to the nonlinear optical properties of HfP_2S_6 is negligible.

Synthesis and stabilization of acentric $Ag_4P_2S_6$.

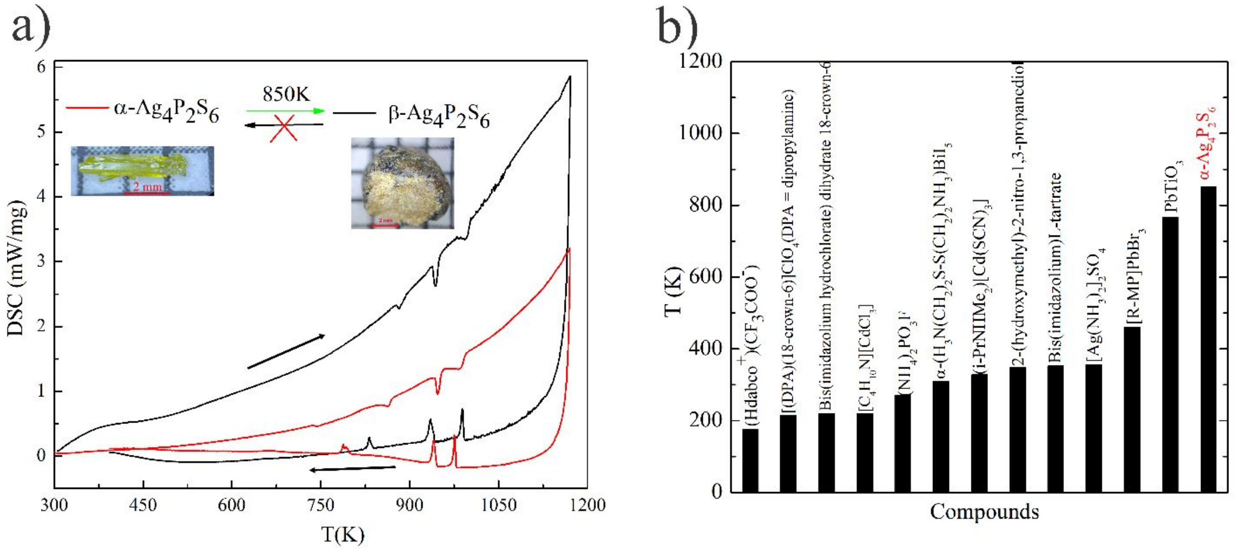

Figure 1. (a) DSC results of non-centrosymmetric $Ag_4P_2S_6$ (α-$Ag_4P_2S_6$, red) and centrosymmetric $Ag_4P_2S_6$ (β-$Ag_4P_2S_6$, black). The insert shows the optical microscope images of α-$Ag_4P_2S_6$ and β-$Ag_4P_2S_6$ crystals and the phase transition relationship between them. (b) A comparison of phase transition temperature between α-$Ag_4P_2S_6$ and selected "optical switch" materials [72-89].

The synthesis of $Ag_4P_2S_6$ is more challenging due to the presence of both centrosymmetric phase (CS-$Ag_4P_2S_6$) and non-centrosymmetric phase (NCS-$Ag_4P_2S_6$)[90, 91]. The CS-$Ag_4P_2S_6$ crystallizes in $P2_1/b$ (No. 14) with unit cell parameters of a= 6.522(4) Å, b= 19.616(8) Å, and c= 11.797(6) Å, and β= 93.58(2)°.[91] The NCS-$Ag_4P_2S_6$ crystallizes in $P2_12_12_1$ (No. 19) with unit cell parameters of a= 13.901(7) Å, b= 11.073(6) Å, and c= 6.303(4) Å[90]. The detailed structure comparison between CS-$Ag_4P_2S_6$ and NCS-$Ag_4P_2S_6$ are summarized in **Figure S3**. Both CS-$Ag_4P_2S_6$ and NCS-$Ag_4P_2S_6$ are constructed with [P_2S_6] motifs and [AgS_4] tetrahedra via sharing vertices and edges. With the removal of Ag atoms, the arrangement of [P_2S_6] motifs within CS-$Ag_4P_2S_6$ and NCS-$Ag_4P_2S_6$ are quite different (**Figures S3 b** and **S3 d**, respectively). The [P_2S_6] motifs are aligned parallel to each other within NCS-$Ag_4P_2S_6$, while the [P_2S_6] motifs within CS-$Ag_4P_2S_6$ are almost perpendicular to each other.

DSC was employed to study the thermal stability of both CS-$Ag_4P_2S_6$ and NCS-$Ag_4P_2S_6$, which are shown in **Figure 1 a**. Both CS-$Ag_4P_2S_6$ and NCS-$Ag_4P_2S_6$ exhibit comprehensive thermal behavior, which are common features of the ternary Ag-P-S system [92]. For NCS-$Ag_4P_2S_6$ sample, there were four endothermic peaks observed during the heating process, located at 730(5) K, 850(5) K, 940(5) K, and 960(5) K. The phase purity of NCS-$Ag_4P_2S_6$ crystals were confirmed by synchrotron powder X-ray diffraction (**Figure S4**) and lab powder X-ray diffraction (**Figure S5**). For CS-$Ag_4P_2S_6$ sample, there were three endothermic peaks observed during the heating process, located at 874(5) K, 937(5) K, and 975(5) K. The cooling down process for NCS-$Ag_4P_2S_6$ sample is similar to CS-$Ag_4P_2S_6$ sample, which both exhibit three exothermic peaks. The first endothermic peak at 730(5) K of NCS-$Ag_4P_2S_6$ sample is corresponding to the melting of amorphous AgBr (melting temperature: 705K). The second endothermic peak at 850(5) K of NCS-$Ag_4P_2S_6$ sample is the process of phase transition from NCS-$Ag_4P_2S_6$ to CS-$Ag_4P_2S_6$. The proofs for this statement are: 1). The PXRD results revealed that NCS-$Ag_4P_2S_6$ sample after DSC treatment were converted to CS-$Ag_4P_2S_6$ (**Figure S6**). CS-$Ag_4P_2S_6$ remained unchanged after DSC process (**Figure S6**). 2). The NCS-$Ag_4P_2S_6$ sample, annealed at 801K, remained the same phase (**Figure S7**). There was a presence of significant amounts of CS-$Ag_4P_2S_6$ crystals in the samples of NCS-$Ag_4P_2S_6$ which annealed at 901K (**Figure S7**). 3). The DSC exhibited comparable signals after 900K. Hence, we determined that centrosymmetric CS-$Ag_4P_2S_6$ is the high temperature stable phase, which is assigned as β-$Ag_4P_2S_6$. The non-centrosymmetric NCS-$Ag_4P_2S_6$ is the low temperature stable phase, which is assigned as α-$Ag_4P_2S_6$. The α-$Ag_4P_2S_6$ possesses type-I phase transition to β-$Ag_4P_2S_6$. The first endothermic peak at 874(5) K of β-$Ag_4P_2S_6$ sample might correspond to its eutectoid temperature, where β-$Ag_4P_2S_6$ sample can be partially transferred to α-$Ag_4P_2S_6$. The proof for this is the synthesis experiment carried at 873 K detected both α-$Ag_4P_2S_6$ and β-$Ag_4P_2S_6$ (**Figure S8**). Beyond 900K, all samples within DSC treatment are β-$Ag_4P_2S_6$. This was supported by synthesis experiments done at 1073 K and 1173K, where only β-$Ag_4P_2S_6$ were the main products. Hence the endothermic peak around 937(5) K for both α-$Ag_4P_2S_6$ and β-$Ag_4P_2S_6$ should correspond to the melting of β-$Ag_4P_2S_6$. The peak which followed the melting of β-$Ag_4P_2S_6$ are unclear so far. The cooling down process is also very comprehensive to interpret. We employed quenching experiments to understand the nature of the cooling down process as shown in **Figure S7**. The sample of α-$Ag_4P_2S_6$ quenched at 1004K was amorphous. The sample of α-$Ag_4P_2S_6$ quenched at 839K was β-$Ag_4P_2S_6$. To better understand the thermal behavior of α-$Ag_4P_2S_6$ and β-$Ag_4P_2S_6$, more experiments such as *in-situ* PXRD are necessary and undergoing.

The phase transition from acentric α-$Ag_4P_2S_6$ to centrosymmetric β-$Ag_4P_2S_6$ upon heating is related to a group of emerging functional materials called optical switch [72-89]. In recent years, the optical switch has been emerging as a new and important research direction [72-89]. **Figure 1b** shows the comparison of phase transition temperature between α-$Ag_4P_2S_6$ and many state-of-the-art optical switch materials. α-$Ag_4P_2S_6$ possesses much higher phase-transition temperature. Please note, however, that all materials in **Figure 1b** are reversible for their CS to NCS transition except α-$Ag_4P_2S_6$, which are necessary for optical switch application. Inorganic compounds have higher phase transition temperatures than hybrid materials. Increasing the reversibility for inorganic compounds is important for their high temperature applications [72-89].

Our initial experiments always made β-$Ag_4P_2S_6$ as the main phase mixed with small amounts of α-$Ag_4P_2S_6$. The efforts of generating a single phase of α-$Ag_4P_2S_6$ via heating elements all failed, where β-$Ag_4P_2S_6$ remained as the major product (**Figure S8**). Phase-pure samples and mm-sized crystals of acentric α-$Ag_4P_2S_6$ were successfully synthesized in AgBr flux as shown in **Figures S2 and S4**. Via employing AgBr flux, high quality single crystals of α-$Ag_4P_2S_6$ can be grown (**Figure S2 right**). The AgBr flux can be removed by centrifuge at high temperature. As shown in **Figures S4**, there is not centrosymmetric β-$Ag_4P_2S_6$ present in our samples. Lab powder X-ray diffraction results also verified the single-phase nature of acentric α-$Ag_4P_2S_6$ in our samples (**Figure S5**). Our nonlinear optical property measurement confirmed the acentric nature of α-$Ag_4P_2S_6$ (*vide infra*). AgBr flux played an important role in stabilizing α-$Ag_4P_2S_6$ regardless of the phase transition between α-$Ag_4P_2S_6$ and β-$Ag_4P_2S_6$.

Crystal Structure.

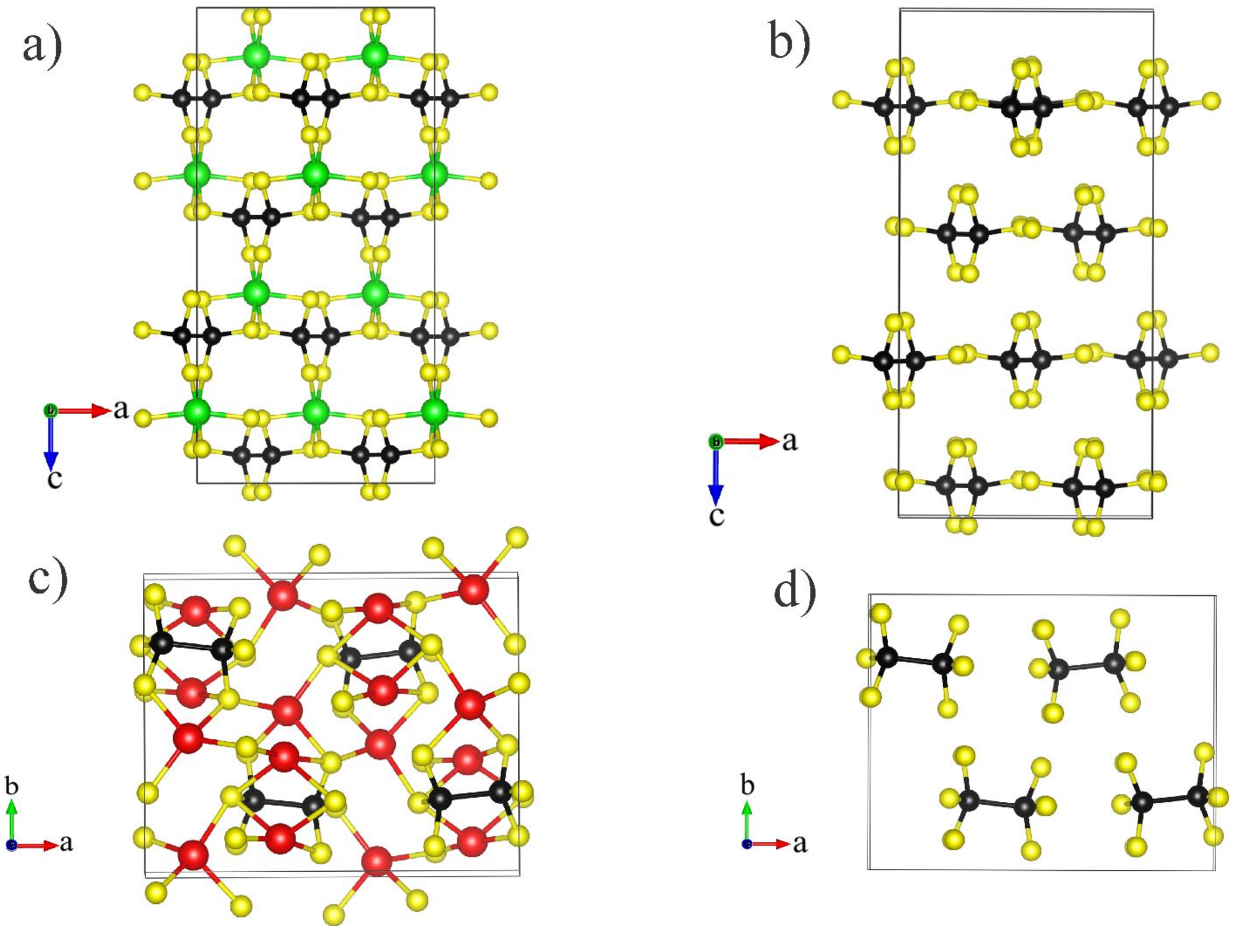

Figure 2. a) ball-stick model of HfP_2S_6 viewed along the [010] direction. b) The arrangement of $[P_2S_6]$ motifs within HfP_2S_6, where Hf atoms are removed for clarity. c) ball-stick model of α-$Ag_4P_2S_6$ viewed along the [001] direction. d) The arrangement of $[P_2S_6]$ motifs within $Ag_4P_2S_6$, where Ag atoms are removed for clarity. Hf: green color, Ag: red color, P: black color, S: yellow color.

The crystal structure of HfP_2S_6 and α-$Ag_4P_2S_6$ are plotted in **Figure 2**. As shown in **Figure 2**, HfP_2S_6 and α-$Ag_4P_2S_6$ are constructed by almost identical $[P_2S_6]$ motifs. The three-dimensional framework of HfP_2S_6 is built by $[HfS_6]$ octahedra interlinked with $[P_2S_6]$ motifs via the sharing of vertices and edges. Hf atoms located in the center of a distorted octahedron have Hf-S interactions falling into the range of 2.527-2.555 Å [71]. The α-$Ag_4P_2S_6$ constitutes a three-dimensional framework constructed by distorted [AgS_4] tetrahedra connected to [P_2S_6] motifs via the sharing of vertices and edges (**Figure 2c**). The Ag-S interactions fall into the range of 2.526-2.942 Å, which confirmed the distorted nature of the [AgS_4] tetrahedra. The bonding pictures of Ag-S interactions were studied by crystal orbitals Hamilton population and electron localization function analysis (*vide infra*). The [P_2S_6] motifs within HfP_2S_6 is almost identical to the [P_2S_6] motifs in α-$Ag_4P_2S_6$. The P-P interactions are 2.253 Å and 2.267 Å for HfP_2S_6 and α-$Ag_4P_2S_6$, respectively. The P-S interactions within HfP_2S_6 are 1.965-2.068 Å, which are comparable to P-S interactions of 2.009-2.057 Å in α-$Ag_4P_2S_6$. The arrangement of [P_2S_6] motifs are different in HfP_2S_6 and α-$Ag_4P_2S_6$ as shown in **Figure 2b** and **Figure 2d**, respectively. Our recent research has demonstrated that the alignment of [P_2S_6] motifs will greatly affect the optical properties of compounds.[49, 50] The alignment of [P_2S_6] motifs within α-$Ag_4P_2S_6$ is more parallel to each other than that of HfP_2S_6. Our experimental NLO properties measurement verified that α-$Ag_4P_2S_6$ possesses much better SHG response than HfP_2S_6 (*vide infra*).

In addition to the almost identical building of [P_2S_6] motifs, the number of electrons transferred from cations to [P_2S_6] motifs are the same for HfP_2S_6 and α-$Ag_4P_2S_6$. The charge-balanced formula of [Hf^{4+}] [P^{4+}]$_2$[S^{2-}]$_6$ and [Ag^+]$_4$[P^{4+}]$_2$[S^{2-}]$_6$ can be established for HfP_2S_6 and α-$Ag_4P_2S_6$, respectively, via the assigning of a formal charge of +4 to the Hf atoms, +1 to the Ag atoms, +4 to the P atoms due to the presence of P-P bonds, and -2 to the S atoms. There is a total of 4 electrons transferred from Hf^{4+} and Ag^+ cations to [P_2S_6] motifs within HfP_2S_6 and α-$Ag_4P_2S_6$, respectively, even though HfP_2S_6 and α-$Ag_4P_2S_6$ crystallize in different structures. The d^0 electron configuration of Hf^{4+} and the d^{10} electron configuration of Ag^+, and their interaction with [P_2S_6] motifs with their affected NLO properties, serves as an interesting topic to study. Due to the more complex crystal structure and highly distorted nature of [AgS_4] tetrahedra within α-$Ag_4P_2S_6$, the bonding pictures of α-$Ag_4P_2S_6$ were studied via COHP coupled with ELF analysis.

Bonding pictures study of α-$Ag_4P_2S_6$.

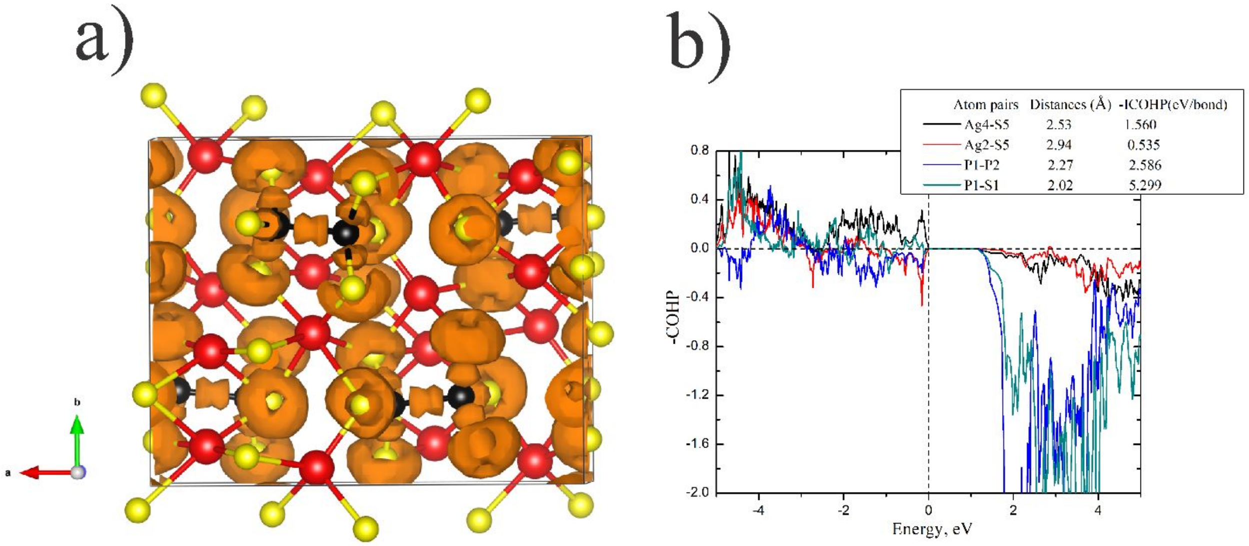

Figure 3. (Left) Electron localization function (ELF, η=0.75) and crystal orbital Hamilton population (COHP) analysis of α-$Ag_4P_2S_6$.

The ELF results and COHP simulation results are presented in **Figure 3a** and **3b**, respectively. As shown in **Figure 3a**, there are no attractors (ELF maximum) located between Ag-S interactions, where all attractors surround S atoms. Hence the Ag atoms are expected to act as cations in α-$Ag_4P_2S_6$. The Ag-S interactions are expected to have ionic interaction features. The Ag-S interactions span a very large range of 2.526-2.942 Å. The calculated –ICOHPs for the 2.53 Å Ag-S interactions are 1.560 eV/bond, which indicate strong ionic bonding characteristics. The calculated –ICOHPs for the 2.94 Å Ag-S interactions are 0.535 eV/bond, which is expected to exhibit weak ionic bonding characteristics. The P-P bonds and P-S bonds are predicated to be covalent bonding in nature with the presence of apparent attractors between P-S bonds and P-P bonds. A similar observation was observed for many compounds, constituting of [P_2S_6] motifs, such as $K_2BaP_2S_6$ [49], $Eu_2P_2S_6$ [53], $RbBiP_2S_6$ [52], $Pb_2P_2S_6$ [50], etc. The 2.27 Å P-P bonds show strong bonding characters with –ICOHPs of 2.586 eV/bond. The ICOHPs for 2.21 Å P-P within β-$Ba_2P_2S_6$ are 2.947 eV/bond [50]. The ICOHPs for 2.22 Å P-P within $KBiP_2S_6$ are 2.698 eV/bond [49]. The P-P interactions within α-$Ag_4P_2S_6$ are 2.27 Å which is comparable with typical homoatomic P-P bond distances such as α-$Ba_2P_2S_6$ (2.213(3) Å) [50], β-$Ba_2P_2S_6$ (2.216(5) Å) [50], $BaCu_5P_3$ (2.263 Å) [93], $Ba_8Cu_{14}Ge_6P_{26}$ (2.265 Å) [94], $La_2Ba_6Cu_{16}P_{30}$ (2.071-2.428 Å) [95], $La_7Zn_2P_{11}$ (2.207(7) Å) [96], and $La_4Zn_7P_{10}$ (2.151(8) Å) [97]. The ICOHPs for 2.02 Å P-S within $Ag_4P_2S_6$ are 5.299 eV/bond, which demonstrate very strong covalent bonding characteristics. A similar bonding picture is also expected for HfP_2S_6.

Electronic Structure.

The electronic structures of HfP_2S_6 and α-$Ag_4P_2S_6$ were studied to understand their electronic properties. The semiconductor natures of HfP_2S_6 and α-$Ag_4P_2S_6$ were confirmed by electronic calculations (**Figure 4**, **Figures S10-S12**). The top of the valance band of α-$Ag_4P_2S_6$ is located at the interval from point Γ to point X in the Brillouin zone. The bottom of the conduction band is located at point Γ in the Brillouin zones (**Figure S9**). Hence, α-$Ag_4P_2S_6$ is predicated to be an indirect bandgap semiconductor of 1.36 eV. HfP_2S_6 is predicated to be an indirect bandgap semiconductor with a calculated bandgap of 2.10 eV, with the top of valance band and the bottom of conduction band located at point Z|L and point Γ, respectively, in the Brillouin zone (**Figure S10**). The calculated bandgap values were verified by experimental UV-Vis results (*vide infra*). To verify the accuracy of DFT calculation results of α-$Ag_4P_2S_6$, tight-binding calculation were employed (**Figures S11** and **S12**). The bandgap calculated from TB-LMTO-ASA is 1.2 eV, which agrees well with 1.36 eV obtained from DFT calculations.

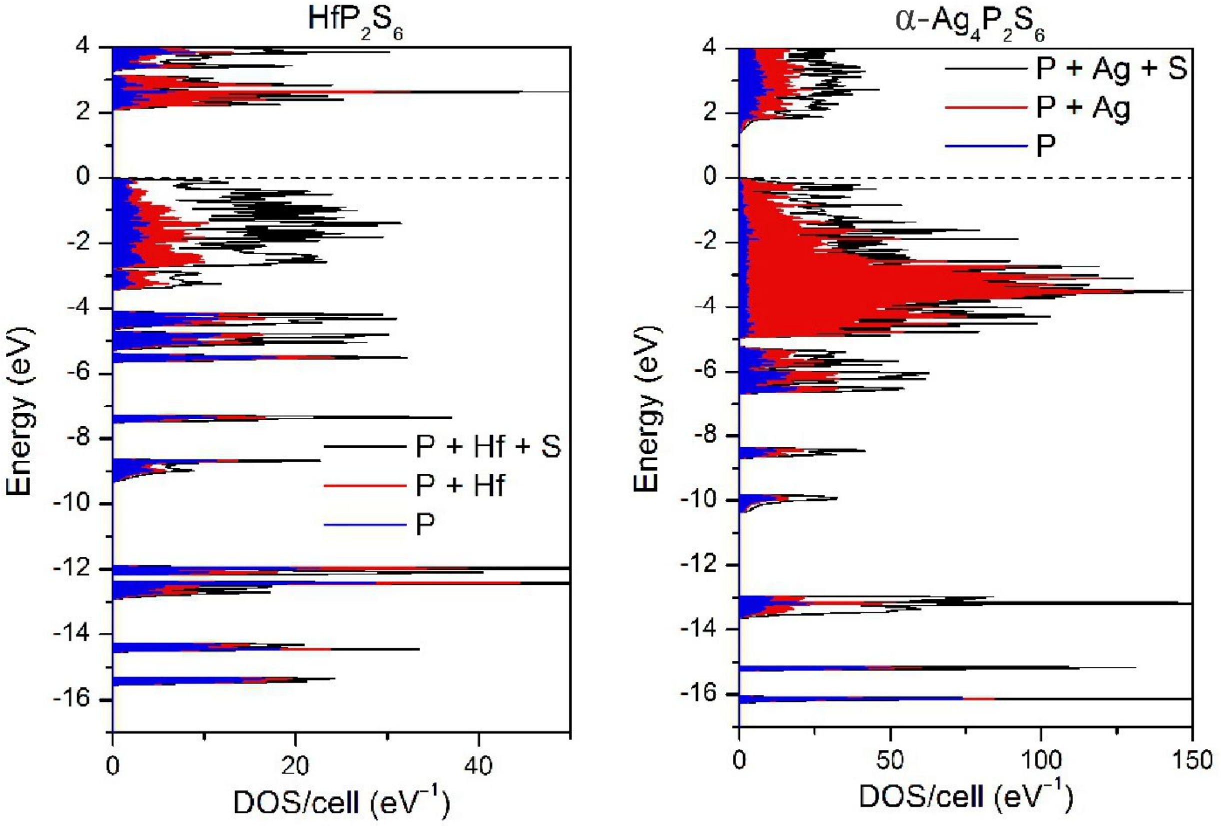

Figure 4. Density of states (DOS) and partial density of states (PDOS) of HfP_2S_6 (left) and $Ag_4P_2S_6$ (right).

For HfP_2S_6, the predominate contribution to the states below the Fermi level are from phosphorous atoms and sulfur atoms. There are very small contributions from Hf atoms to the states below the Fermi level. In contrast, orbitals from Hf atoms dominate the contributions of the bottom of conduction bands, where the P atoms and S atoms also have certain contributions. The orbitals from Hf atoms mainly populate around 2-3 eV and (-1eV)-(-3.2 eV) which indicates that Hf significantly contributes to the optical properties of HfP_2S_6. Overall, the optical properties of HfP_2S_6 will dominantly be contributed by Hf-S and P-S interactions. α-$Ag_4P_2S_6$ has a different story when compared with HfP_2S_6. The top of the conduction band of α-$Ag_4P_2S_6$ has dominant contributions from the Ag-4d and S-3p orbitals. There is very negligible contribution from P-3p orbitals to the top of the conduction bands. Ag-4d orbitals and S-3p orbitals are also major contributors to the bottom of the conduction band, where the P-3p orbitals have some contributions. Hence, the optical properties of α-$Ag_4P_2S_6$ are mainly contributed from $[AgS_4]$ tetrahedra, with certain contributions from $[P_2S_6]$ motifs. The Ag-4d orbitals are mainly localized in the energy region from 0 eV-(-5 eV), while the Ag-4s orbitals are mainly localized at the bottom of the conduction band. Hence, the oxidation states of Ag is expected to be +1 [93]. The contribution of electron density from Ag-4d orbitals increases the total density of states of α-$Ag_4P_2S_6$ to 120 eV/cell, at the vicinity of around -3 eV. HfP_2S_6 has a much smaller total density of states of 12 eV/cell at the same energy point. From electronic structure calculations, we anticipate HfP_2S_6 and α-$Ag_4P_2S_6$ would exhibit different optical properties regardless of the same structural $[P_2S_6]$ motifs.

Linear optical properties.

The optical bandgaps of HfP_2S_6 and α-$Ag_4P_2S_6$ were evaluated by solid-state UV−vis Kubelka−Munk (KM) diffuse reflectance spectroscopy as summarized in **Table 1**. As shown in **Figure S13**, there are strong absorptions around 500-550 nm and 600-650 nm for HfP_2S_6 and α-$Ag_4P_2S_6$, respectively. HfP_2S_6 and α-$Ag_4P_2S_6$ are predicated to be indirect bandgap semiconductors via VASP calculations. The allowed indirect transition estimated by the Tauc plots for HfP_2S_6 and α-$Ag_4P_2S_6$ are 2.2(1) eV and 2.5(1) eV, respectively (**Figures S14 and S15**). The experimentally estimated bandgap of HfP_2S_6 agrees well with theory calculation results, 2.1 eV and 2.2(1) eV, respectively. The experimentally estimated bandgap of α-$Ag_4P_2S_6$ is significantly higher than the theory calculation results, 1.4 eV and 2.5(1) eV, respectively. The underestimation of bandgaps of Ag-containing compounds is common in literatures, which originates from the limitation of DFT calculation methods and particularity of the Ag^+ cations [7]. For an example, the calculated bandgap of $AgGaS_2$ varies from 0.86 eV to 2.2 eV, where the experimental bandgap of $AgGaS_2$ is 2.7 eV [98, 99]. Another example is Ag_3PS_4, where the calculated bandgap and experimental bandgap are 1.7 eV [100] and 2.4 eV [38], respectively. The bandgap for HfP_2S_6 and α-$Ag_4P_2S_6$ are comparable to $AgGaS_2$ (2.7 eV). Due to the potential "switch" application between α-$Ag_4P_2S_6$ and β-$Ag_4P_2S_6$, the bandgap of β-$Ag_4P_2S_6$ was also evaluated by UV-Vis measurements as shown in **Figures S16** and **S17**. β-$Ag_4P_2S_6$ possess comparable bandgap with α-$Ag_4P_2S_6$. The direct and indirect bandgaps for β-$Ag_4P_2S_6$ are 2.9(1) eV and 2.5(1) eV, respectively. The IR spectrum of HfP_2S_6, α-$Ag_4P_2S_6$, and β-$Ag_4P_2S_6$ were measured and presented in **Figure S18**, where high similarity of the IR spectrum was observed for these three compounds. The IR spectrum did not show any intrinsic vibrational absorption of chemical bonds in the wavelength of 2.5–18.2 μm. The only strong absorption at 550 cm^{-1} can be assigned to the ν (P–S) vibrations [101]. The IR spectrum of HfP_2S_6, α-$Ag_4P_2S_6$, and β-$Ag_4P_2S_6$ is comparable to many thiophosphates such as $AgCd_3PS_6$ [42], KAg_2PS_4 [56], $Sn_2P_2S_6$ [47], and $AgHgPS_4$ [102].

Table 1. Summary of linear optical properties of HfP_2S_6 and α-$Ag_4P_2S_6$

	HfP_2S_6	α-$Ag_4P_2S_6$
Direct allowed transition	2.6(1) eV	2.7(1) eV
Indirect allowed transition	2.2(1) eV	2.5(1) eV
DFT calculations	2.1 eV	1.4 eV
LMTO calculations	N/A	1.2 eV

Nonlinear optical properties.

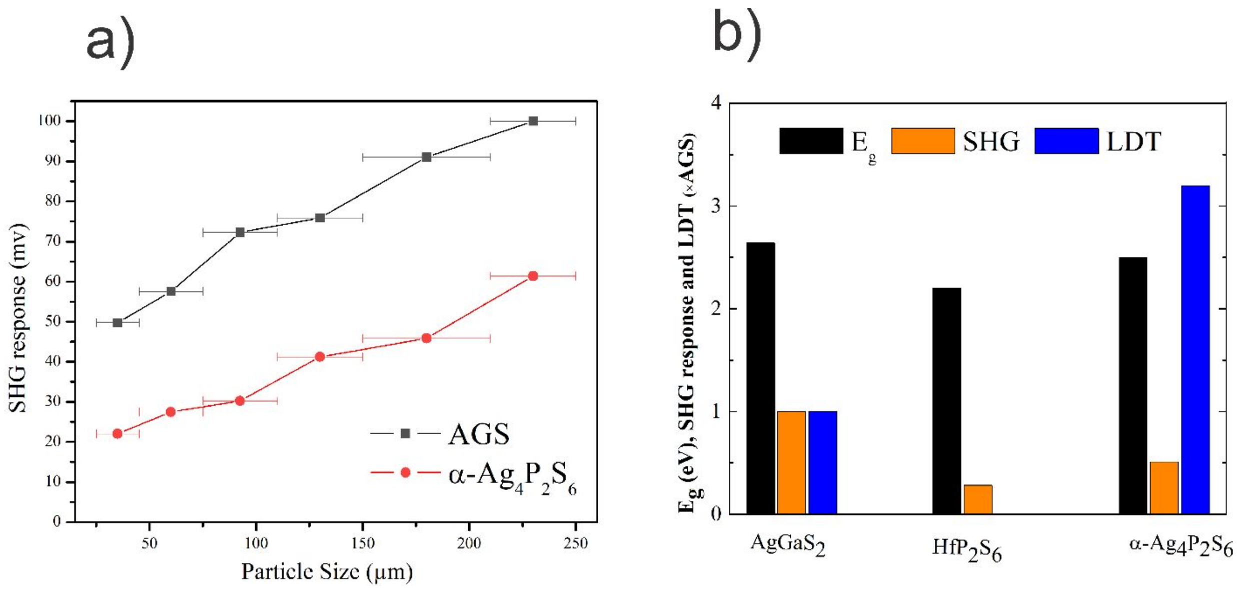

Figure 5. (a) SHG intensities of α-$Ag_4P_2S_6$ and $AgGaS_2$ were measured with variable particle sized samples, utilizing a 2.09 μm laser. (b) The comparison of the bandgap (E_g), SHG response (×$AgGaS_2$ based on 25 μm particle size samples), and LDT (×$AgGaS_2$) between $AgGaS_2$, α-$Ag_4P_2S_6$, and HfP_2S_6.

Nonlinear optical properties of HfP_2S_6 and α-$Ag_4P_2S_6$ were measured and summarized in **Figures 5** and **S19**. The crystal structure features of HfP_2S_6, such as [P_2S_6] motifs perpendicular to each other, coupled with the low density of states, may point to the low SHG response of HfP_2S_6. The experimental results confirmed that HfP_2S_6 exhibits low SHG response. HfP_2S_6 is not a type-I phase-matching material. For the sample of particle size of 25 μm, the SHG of HfP_2S_6 is ~0.21×AGS. In contract to HfP_2S_6, the [P_2S_6] motifs are parallel to each other within α-$Ag_4P_2S_6$. α-$Ag_4P_2S_6$ exhibits much better SHG response (**Figure 5a**). α-$Ag_4P_2S_6$ is a type-I phase-matching material, where the SHG intensity increases with increasing particle size. The phase-matching capability of α-$Ag_4P_2S_6$ is supported by calculated birefringence results (**Figure S20**). α-$Ag_4P_2S_6$ crystals exhibit moderate birefringence. For an incident laser of 2 μm, Δn is 0.13 for α-$Ag_4P_2S_6$. As shown in **Figure S21,** HfP_2S_6 exhibits larger birefringence than α-$Ag_4P_2S_6$. For an incident laser of 2 µm, Δn is 0.25 for HfP_2S_6. The experimental results indicate that HfP_2S_6 is not a phase-matching material, which may originate from the strong absorption and the presence of small amounts of HfS_2 impurity [103,104]. The SHG response of α-$Ag_4P_2S_6$ is about ~0.61×AGS for the sample of particle size of 225 µm. More importantly, α-$Ag_4P_2S_6$ has a high LDT of ~3.2×AGS (**Table S1**). α-$Ag_4P_2S_6$ is a good candidate for infrared nonlinear optical applications due to moderate SHG response, high LDT, comparable bandgaps with AGS, extraordinary ambient stability, and the ease to grow large crystals. The phase transition between acentric α-$Ag_4P_2S_6$ and centrosymmetric β-$Ag_4P_2S_6$ may also find application as optical switches.

Photocurrent response of α-$Ag_4P_2S_6$ and β-$Ag_4P_2S_6$.

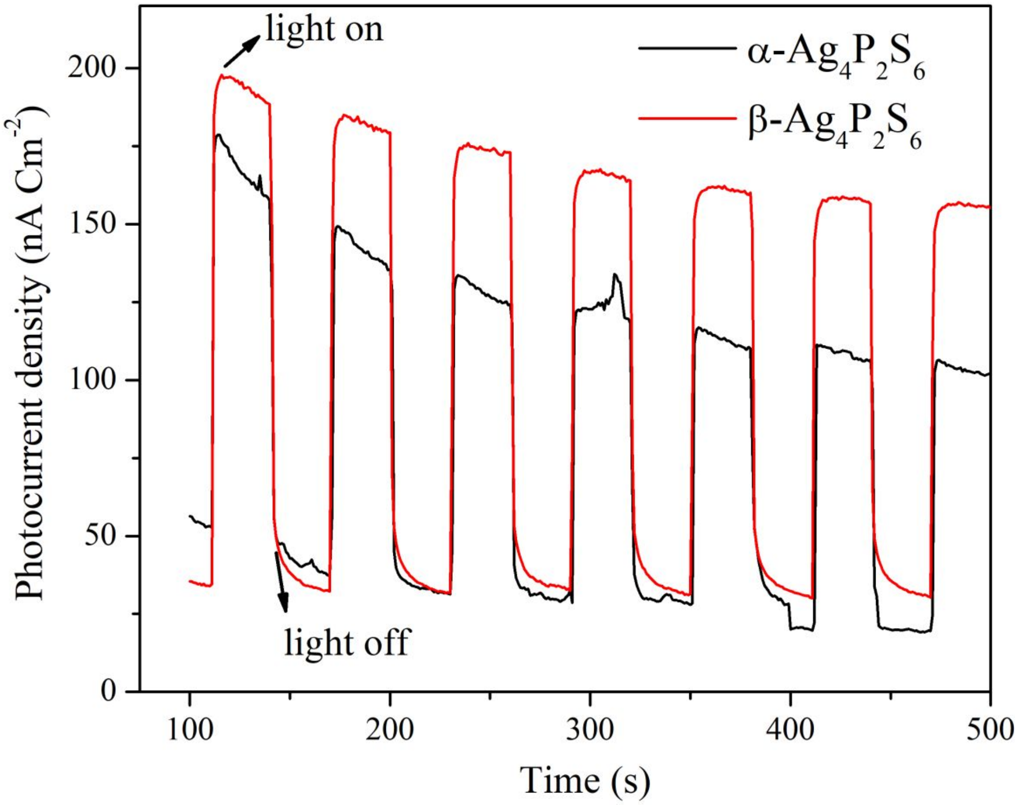

Figure 6. Photocurrent density of α-$Ag_4P_2S_6$ and β-$Ag_4P_2S_6$ photoanodes over time.

Studying physical properties of polymorphs is always an important topic for materials research [50, 105-108]. Photovoltaic materials can directly covert light into electricity, which can reduce our dependence of fossil energy [109-111]. Exploring new materials with good photocurrent response is also in our research interests [51]. Hence, in this work, we measured the photocurrent response of α-$Ag_4P_2S_6$ and β-$Ag_4P_2S_6$, which are summarized in **Figure 6**. Both α-$Ag_4P_2S_6$ and β-$Ag_4P_2S_6$ exhibit good photocurrent response. α-$Ag_4P_2S_6$ and β-$Ag_4P_2S_6$ also show good reproducibility of photocurrent response as shown in **Figures S22** and **S23**. Several repeatable on-off cycles indicate that α-$Ag_4P_2S_6$ and β-$Ag_4P_2S_6$ are n-type semiconductors. The photocurrent slightly decreases after a few cycles, which originates from the photocorrosion of a sulfide photocatalyst [112, 113]. In contrast to nonlinear optical properties, β-$Ag_4P_2S_6$ possesses better photocurrent response than α-$Ag_4P_2S_6$. The photocurrent density of α-$Ag_4P_2S_6$ and β-$Ag_4P_2S_6$ are 165 nA cm^{-2} and 135 nA cm^{-2}, respectively. A comparison of photocurrent response among α-$Ag_4P_2S_6$, β-$Ag_4P_2S_6$ and many previously reported sulfides are summarized in **Table S2** [51, 114-124]. α-$Ag_4P_2S_6$ and β-$Ag_4P_2S_6$ show better photocurrent response than many sulfides such as $BaCuSbS_3$ (55 nA cm^{-2}) [121], $Cs_2Ag_2Zn_2S_4$(50 nA cm^{-2}) [122], $Rb_2Ba_3Cu_2Sb_2S_{10}$ (6 nA cm^{-2}) [123], and $TlHgInS_3$ (0.35 nA cm^{-2}) [124]. α-$Ag_4P_2S_6$ is a multifunctional material which combines moderate NLO properties and photocurrent response. The polymorphism study of α-$Ag_4P_2S_6$ and β-$Ag_4P_2S_6$ also demonstrates the rich structural chemistry of the ternary Ag-P-S system. Another emerging multifunctional material of the ternary Ag-P-S system is Ag_3PS_4, which is a good ion conductor and NLO material [38, 125]. New multifunctional materials are possible to be found within the ternary Ag-P-S system.

Conclusions

Two structurally known thiophosphates, HfP_2S_6 and α-Ag_4P_2S6, are evaluated as potential infrared nonlinear optical materials. HfP_2S_6 and α-$Ag_4P_2S_6$ were synthesized via high temperature salt flux method. α-$Ag_4P_2S_6$ were grown as high-quality mm-sized crystals with the aid of AgBr flux, which were eliminated by the centrifuge methods. The acentric α-$Ag_4P_2S_6$ transfers to centrosymmetric β-$Ag_4P_2S_6$ at 850(5) K, which were revealed by DSC measurements and synthetic experiments. There was no phase transition detected transferring from β-$Ag_4P_2S_6$ to α-$Ag_4P_2S_6$. Both HfP_2S_6 and α-$Ag_4P_2S_6$ are constructed by [P_2S_6] motifs interconnected by [HfS_6] octahedron and [AgS_4] tetrahedron, respectively. The bonding picture study reveals the strong ionic bonding nature of Ag-S interactions, the strong covalent bonding nature of P-P interactions, and P-S interactions within α-$Ag_4P_2S_6$. Both HfP_2S_6 and α-$Ag_4P_2S_6$ are discovered as indirect bandgap semiconductors of bandgaps of 2.1 eV and 1.4 eV, respectively by DFT calculations. The experimental bandgaps obtained from UV-Vis test are 2.2(1) eV and 2.5(1) eV for HfP_2S_6 and α-$Ag_4P_2S_6$, respectively. HfP_2S_6 exhibits low SHG response, ~0.21×AGS. α-$Ag_4P_2S_6$ owns moderate SHG response, ~0.61×AGS coupled with a high LDT of ~3.2×AGS. α-$Ag_4P_2S_6$ and β-$Ag_4P_2S_6$ possess good photocurrent response. The photocurrent density of α-$Ag_4P_2S_6$ and β-$Ag_4P_2S_6$ are 165 nA cm^{-2} and 135 nA cm^{-2}, respectively. α-$Ag_4P_2S_6$ possesses good potential as infrared NLO materials due to its high ambient stability, moderate SHG response and bandgap, type-I phase-matching behavior, high LDT, and easy to grow large crystals. α-$Ag_4P_2S_6$ is a multifunctional material which combines moderate NLO properties and photocurrent response.

Associated contents:

Supporting Information

The lab X-ray diffraction and 11-BM diffraction results, microscope photo of crystals, UV-Vis results and Tauc plots, Calculated band structure, Tb-LMTO-ASA calculation results, SHG and LDT results, photocurrent response test, photocurrent response of selected sulfides.

Notes: #C. C and B. J equally contributed to this work. The authors declare no competing financial interest.

Funding: This research was supported by start-up funds from Wichita State University. W. W would like to thanks supports from the ACS Petroleum Research Fund (PRF #59716-DNI10) and The Kansas NASA EPSCoR Research Infrastructure Development Program (#80NSSC19M0042).

Acknowledgments: J.W would like to thank Kui Wu, at Hebei University, for helping with the LDT measurement and Guangmao Li, at Xinjiang Technical Institute of Physics & Chemistry of CAS, for helping with the SHG measurement. Use of the Advanced Photon Source, an Office of Science User Facility operated for the U.S. Department of Energy (DOE) Office of Science by Argonne National Laboratory, was supported by the U.S. DOE under Contract No. DE-AC02−06CH11357.

Corresponding author:

Jian Wang jian.wang@wichita.edu

References:

[1] C. T. Chen, B. C. Wu, A. D. Jiang and G. M. You, *Sci. China Ser.*, 1985, **28**, 235–243.

[2] C. Chen, Y. Wu, A. Jiang, B. Wu, G. You, R. Li and S. Lin, *J. Opt. Soc. Am. B*, 1989, **6**, 616.

[3] Z.-X. Chen, W. Liu and S.-P. Guo, *Coord. Chem. Rev.*, 2023, **474**, 214870.

[4] V. G. Dmitriev, G. G. Gurzadyan and D. N. Nikogosyan, *Handbook of nonlinear optical crystals*, Springer Berlin Heidelberg, Berlin, Heidelberg, 1999.

[5] T. A. Driscoll, H. J. Hoffman, R. E. Stone and P. E. Perkins, *J. Opt. Soc. Am. B, JOSAB*, 1986, **3**, 683–686.

[6] C. Chen, Y. Wang, B. Wu, K. Wu, W. Zeng and L. Yu, *Nature*, 1995, **373**, 322–324.

[7] L. Kang, M. Zhou, J. Yao, Z. Lin, Y. Wu and C. Chen, *J. Am. Chem. Soc.*, 2015, **137**, 13049–13059.

[8] H. Zhang, M. Zhang, S. Pan, X. Dong, Z. Yang, X. Hou, Z. Wang, K. B. Chang and K. R. Poeppelmeier, *J. Am. Chem. Soc.*, 2015, **137**, 8360–8363.

[9] H. Yu, J. Young, H. Wu, W. Zhang, J. M. Rondinelli and P. S. Halasyamani, *J. Am. Chem. Soc.*, 2016, **138**, 4984–4989.

[10] I. Chung and M. G. Kanatzidis, *Chem. Mater.*, 2014, **26**, 849–869.

[11] T. K. Bera, J. I. Jang, J. B. Ketterson and M. G. Kanatzidis, *J. Am. Chem. Soc.*, 2009, **131**, 75–77.

[12] F. Liang, L. Kang, Z. Lin and Y. Wu, *Cryst. Growth Des.*, 2017, **17**, 2254–2289.

[13] A. Abudurusuli, J. Li and S. Pan, *Dalton Trans.*, 2021, **50**, 3155–3160.

[14] D. Chu, C. Xie and Z. Yang, *Inorg. Chem.*, 2022, **61**, 11454–11462.

[15] G. Li, Z. Yang, J. Li and S. Pan, *Chem. Commun.*, 2020, **56**, 11565–11576. [16] G. Cicirello, K. Wu, B. B. Zhang and J. Wang, *Inorg. Chem. Front.*, 2021, **8**, 4914–4923.

[17] B. Ji, K. Pandey, C. P. Harmer, F. Wang, K. Wu, J. Hu and J. Wang, *Inorg. Chem.*, 2021, **60**, 10603–10613.

[18] G. Cicirello, K. Wu and J. Wang, *J. Solid State Chem.*, 2021, **300**, 122226.

[19] B. Ji, K. Wu, Y. Chen, F. Wang, A. J. Rossini, B. Zhang and J. Wang, *Inorg. Chem.*, 2022, **61**, 2640–2651.

[20] Z. Ye, S. Bardelli, K. Wu, A. Sarkar, A. Swindle and J. Wang, *Anorg. Allge. Chem.*, 2022, **648**, e202100271.

[21] S. Bardelli, Z. Ye, F. Wang, B. Zhang and J. Wang, *Anorg. Allge. Chem.*, 2022, **648**, e202100388.

[22] R. Wang, F. Liang and Z. Lin, *Sci. Rep.*, 2020, **10**, 3486.

[23] W. Cai, A. Abudurusuli, C. Xie, E. Tikhonov, J. Li, S. Pan and Z. Yang, *Adv. Funct. Mater.*, 2022, **32**, 2200231.

[24] H. Lan, F. Liang, X. Jiang, C. Zhang, H. Yu, Z. Lin, H. Zhang, J. Wang and Y. Wu, *J. Am. Chem. Soc.*, 2018, **140**, 4684–4690.

[25] X. Luo, Z. Li, Y. Guo, J. Yao and Y. Wu, *J. Solid State Chem.*, 2019, **270**, 674–687.

[26] H. Lin, L. Chen, L.-J. Zhou and L.-M. Wu, *J. Am. Chem. Soc.*, 2013, **135**, 12914–12921.

[27] Q.-Q. Liu, X. Liu, L.-M. Wu and L. Chen, *Angew. Chem. Int. Ed Engl.*, 2022, **61**, e202205587.

[28] X.-T. Wu and L. Chen, Eds., *Structure-property relationships in non-linear optical crystals II*, Springer Berlin Heidelberg, Berlin, Heidelberg, 2012.

[29] Z.-Z. Luo, C.-S. Lin, H.-H. Cui, W.-L. Zhang, H. Zhang, H. Chen, Z.-Z. He and W.-D. Cheng, *Chem. Mater.*, 2015, **27**, 914–922.

[30] S.-F. Li, X.-M. Jiang, Y.-H. Fan, B.-W. Liu, H.-Y. Zeng and G.-C. Guo, *Chem. Sci.*, 2018, **9**, 5700–5708.

[31] Z. Li, J. Yao and Y. Wu, *Cryst. Growth Des.*, 2020, **20**, 7550–7564.

[32] X. Chen and K. M. Ok, *Chem. Asian J.*, 2020, **15**, 3709–3716.

[33] Q. Hu, K. Ruan, Y. Wang, K. Ding and Y. Xu, *New J Chem*, 2019, **43**, 12468–12474.

[34] B.-W. Liu, H.-Y. Zeng, X.-M. Jiang, G.-E. Wang, S.-F. Li, L. Xu and G.-C. Guo, *Chem. Sci.*, 2016, **7**, 6273–6277.

[35] M. Zhou, L. Kang, J. Yao, Z. Lin, Y. Wu and C. Chen, *Inorg. Chem.*, 2016, **55**, 3724–3726.

[36] Z. Li, S. Zhang, Z. Huang, L.-D. Zhao, E. Uykur, W. Xing, Z. Lin, J. Yao and Y. Wu, *Chem. Mater.*, 2020, **32**, 3288–3296.

[37] F. Menzel, W. Brockner and W. Carrillo-Cabrera, *Heteroat. Chem.*, 1993, **4**, 393–398.

[38] Y. Yang, B. Zhang, X. Wu and K. Wu, *Dalton Trans.*, 2021, **50**, 4129–4132.

[39] J. Feng, C.-L. Hu, B. Li and J.-G. Mao, *Chem. Mater.*, 2018, **30**, 3901–3908.

[40] J. Feng, C.-L. Hu,X. Xu, B.-X. Li, M.-J. Zhang, J.-G. Mao. *Chem. Eur. J.* 2017, **23**, 10978 – 10982.

[41] Z. Li, S. Zhang, W. Xing, Y. Guo, C. Li, Z. Lin, J. Yao and Y. Wu, *J. Mater. Chem. C Mater. Opt. Electron. Devices*, 2020, **8**, 5020–5024.

[42] Y.-H. Fan, X.-M. Jiang, B.-W. Liu, S.-F. Li, W.-H. Guo, H.-Y. Zeng, G.-C. Guo and J.-S. Huang, *Inorg. Chem.*, 2017, **56**, 114–124.

[43] Z. Li, X. Jiang, M. Zhou, Y. Guo, X. Luo, Y. Wu, Z. Lin and J. Yao, *Inorg. Chem.*, 2018, **57**, 10503–10506.

[44] Y. Chu, P. Wang, H. Zeng, S. Cheng, X. Su, Z. Yang, J. Li and S. Pan, *Chem. Mater.*, 2021, **33**, 6514–6521.

[45] A. Anema, A. Grabar and T. Rasing, *Ferroelectrics*, 1996, **183**, 181–183.

[46] J. He, S. H. Lee, F. Naccarato, G. Brunin, R. Zu, Y. Wang, L. Miao, H. Wang, N. Alem, G. Hautier, G.-M. Rignanese, Z. Mao and V. Gopalan, *ACS Photonics*, 2022, **9**, 1724–1732.

[47] Z.-H. Shi, M. Yang, W.-D. Yao, W. Liu and S.-P. Guo, *Inorg. Chem.*, 2021, **60**, 14390–14398.

[48] V. Manriquez, A. Galdámez, D. R. León, M. T. Garland and M. Jiménez, *Z. Krist. - New Cryst. Struct.*, 2003, **218**, 151–252.

[49] V. Nguyen, B. Ji, K. Wu, B. Zhang and J. Wang, *Chem. Sci.*, 2022, **13**, 2640–2648.

[50] B. Ji, A. Sarkar, K. Wu, A. Swindle and J. Wang, *Dalton Trans.*, 2022, **51**, 4522–4531.

[51] B. Ji, E. Guderjahn, K. Wu, T. H. Syed, W. Wei, B. Zhang and J. Wang, *Phys. Chem. Chem. Phys.*, 2021, **23**, 23696–23702.

[52] M.-M. Chen, S.-H. Zhou, W. Wei, M.-Y. Ran, B. Li, X.-T. Wu, H. Lin and Q.-L. Zhu, *ACS Materials Lett.*, 2022, **4**, 1264–1269.

[53] X. Huang, S.-H. Yang, X.-H. Li, W. Liu and S.-P. Guo, *Angew. Chem. Int. Ed Engl.*, 2022, **61**, e202206791.

[54] L.-J. Yao, C.-L. Hu, Z. Fang and J.-G. Mao, *J. Solid State Chem.*, 2022, **315**, 123433.

[55] Y. Huang, J. Huang and Y. Zhang, *Dalton Trans.*, 2022, **51**, 15067–15073.

[56] W. Zhou, B. Li, W. Liu and S.-P. Guo, *Inorg. Chem. Front.*, 2022, **9**, 4990–4998.

[57] S. K. Kurtz and T. T. Perry, *J. Appl. Phys.*, 1968, **39**, 3798–3813.

[58] G. Kresse and J. Hafner, *Phys. Rev. B Condens. Matter*, 1993, **47**, 558–561.

[59] G. Kresse and J. Hafner, *Phys. Rev. B Condens. Matter*, 1994, **49**, 14251–14269.

[60] G. Kresse and J. Furthmüller, *Comput. Mater. Sci.*, 1996, **6**, 15–50.

[61] G. Kresse and J. Furthmüller, *Phys. Rev. B Condens. Matter*, 1996, **54**, 11169–11186.

[62] G. Kresse and D. Joubert, *Phys. Rev. B Condens. Matter*, 1999, **59**, 1758–1775.

[63] J. P. Perdew, K. Burke and M. Ernzerhof, *Phys. Rev. Lett.*, 1996, **77**, 3865–3868.

[64] H. J. Monkhorst and J. D. Pack, *Phys. Rev. B*, 1976, **13**, 5188–5192.

[65] W. Setyawan and S. Curtarolo, *Comput. Mater. Sci.*, 2010, **49**, 299–312.

[66] B. G. Pfrommer, M. Côté, S. G. Louie, M. L. Cohen. *J. Comput. Phys.* 1997, **131** (1), 233–240.

[67] J. Heyd, G. E. Scuseria. *J. Chem. Phys.* 2003,**118,** 8207.

[68] A. V. Krukau, O. A. Vydrov, A. F. Izmaylov, G. E. Scuseria. *J. Chem. Phys.* 2006, **125**, 224106.

[69] R. Tank, O. Jepsen and A. Burkhardt, The Program TB-LMTO-ASA. Version 4.7. *Max-Planck-Inst. Festkorperforschung Stuttg. Ger.* **1999**.

[70] U. von Barth and L. Hedin, *J. Phys. C Solid State Phys.* 1972*,* **5** (13), *1629–1642.*

[71] A. Simon, H. Hahn and K. Peters, *Z. Naturforsch. B J. Chem. Sci.*, 1985, **40**, 730–732.

[72] W. Bi, N. Louvain, N. Mercier, J. Luc, I. Rau, F. Kajzar and B. Sahraoui, *Adv. Mater.*, 2008, **20**, 1013–1017.

[73] Z. Sun, S. Li, S. Zhang, F. Deng, M. Hong and J. Luo, *Adv. Opt. Mater.*, 2014, **2**, 1199–1205.

[74] C. Ji, Z. Sun, S. Zhang, S. Zhao, T. Chen, Y. Tang and J. Luo, *Chem. Commun. (Camb.)*, 2015, **51**, 2298–2300.

[75] Z. Sun, T. Chen, C. Ji, S. Zhang, S. Zhao, M. Hong and J. Luo, *Chem. Mater.*, 2015, **27**, 4493–4498.

[76] Z. Sun, T. Chen, X. Liu, M. Hong and J. Luo, *J. Am. Chem. Soc.*, 2015, **137**, 15660–15663.

[77] Z. Sun, J. Luo, S. Zhang, C. Ji, L. Zhou, S. Li, F. Deng and M. Hong, *Adv. Mater.*, 2013, **25**, 4159–4163.

[78] W.-J. Xu, C.-T. He, C.-M. Ji, S.-L. Chen, R.-K. Huang, R.-B. Lin, W. Xue, J.-H. Luo, W.-X. Zhang and X.-M. Chen, *Adv. Mater.*, 2016, **28**, 5886–5890.

[79] S.-Y. Zhang, X. Shu, Y. Zeng, Q.-Y. Liu, Z.-Y. Du, C.-T. He, W.-X. Zhang and X.-M. Chen, *Nat. Commun.*, 2020, **11**, 2752.

[80] C.-Y. Pan, X.-R. Yang, L. Xiong, Z.-W. Lu, B.-Y. Zhen, X. Sui, X.-B. Deng, L. Chen and L.-M. Wu, *J. Am. Chem. Soc.*, 2020, **142**, 6423–6431.

[81] Y.-C. Yang, X. Liu, X.-B. Deng, L.-M. Wu and L. Chen, *JACS Au*, 2022, **2**, 2059–2067.

[82] H. Peng, Y.-H. Liu, X.-Q. Huang, Q. Liu, Z.-H. Yu, Z.-X. Wang and W.-Q. Liao, *Mater. Chem. Front.*, 2021, **5**, 4756–4763.

[83] Y.-K. Li, Y.-Y. Lai, T.-T. Ying, D.-C. Han, Y.-H. Tan, Y.-Z. Tang, P.-K. Du and H. Zhang, *Chem. Sci.*, 2021, **12**, 13061–13067.

[84] Y. He, Z. Chen, X. Chen, X.-M. Zhang and D. Fu, *Mater. Chem. Front.*, 2022, **6**, 1292–1300.

[85] K. Han, Z. Wei, X. Ye, B. Li, P. Wang and H. Cai, *Dalton Trans.*, 2022, **51**, 8273–8278.

[86] H. Peng, Q. Liu, Y. Liu, Y. Lu and W. Liao, *Chin. Chem. Lett.*, 2022, 107980.

[87] P. Wang, M. Zhang, Z. Wei, W. Du, Z. Peng and H. Cai, *Inorg. Chem.*, 2022, **61**, 16414–16420.

[88] M. C. Oliveira, R. A. P. Ribeiro, E. Longo, M. R. D. Bomio, F. V. Motta and S. R. Lazaro, *Int. J. Quantum Chem.*, 2020, **1**, e26054.

[89] V. Železný, D. Chvostová, D. Šimek, F. Máca, J. Mašek, N. Setter and Y. Hong Huang, *J. Phys. Condens. Matter*, 2016, **28**, 025501

[90] P. Toffoli, P. Khodadad and N. Rodier, *Acta Crystallogr. C*, 1983, **39**, 1485–1488.

[91] P. Toffoli, A. Michelet, P. Khodadad and N. Rodier, *Acta Crystallogr. B*, 1982, **38**, 706–710.

[92] H. Andrae and R. Blachnik, *J. Therm. Anal. Calorim.*, 1989, **35**, 595–607.

[93] G. Cicirello, A. Swindle and J. Wang, *J. Solid State Chem.*, 2021, **296**, 122017.

[94] J. Wang, O. I. Lebedev, K. Lee, J.-A. Dolyniuk, P. Klavins, S. Bux and K. Kovnir, *Chem. Sci.*, 2017, **8**, 8030–8038.

[95] J. Wang, Y. He, N. E. Mordvinova, O. I. Lebedev and K. Kovnir, *Chem*, 2018, **4**, 1465–1475.

[96] J. Wang, P. Yox, J. Voyles and K. Kovnir, *Cryst. Growth Des.*, 2018, **18**, 4076–4083.

[97] J. Wang, K. Lee and K. Kovnir, *Inorg. Chem.*, 2017, **56**, 783–790.

[98] L. Bai, Z. Lin, Z. Wang, C. Chen and M.-H. Lee, *J. Chem. Phys.*, 2004, **120**, 8772–8778.

[99] M. Purohit, S. K. Meena, A. Dashora and B. L. Ahuja, in *Intelligent Computing Techniques for Smart Energy Systems*, Springer Singapore, Singapore, 2020, pp. 67–74.

[100] A. H. Reshak and S. Azam, *J Material Sci Eng*, 2014, **3**, 2169–0022.

[101] S. Banerjee, C. D. Malliakas and M. G. Kanatzidis. *Inorg. Chem.* 2012, **51**, 11562–11573.

[102] W. Xing, N. Wang, C. Tang, C. Li, Z. Lin, J. Yao, W. Yin and B. Kang. *J. Mater. Chem. C,* 2021, **9**, 1062-1068.

[103] B. Ji, F. Wang, K. Wu, B. Zhang and J. Wang. *Inorg. Chem.* 2022. https://doi.org/10.1021/acs.inorgchem.2c03852.

[104] D.J. Clark, J.-H. Zhang, A.J. Craig, A. Weiland, J.A. Brant, J.B. Cho, Y.S. Kim, J. I. Jang and J. A. Aitken *J. Alloys Compd.* 2022, **917**, 165381.

[105] B. Fultz, *Phase Transitions in Materials*, Cambridge University Press, Cambridge, England, 2020.

[106] A. Balvanz, S. Baranets, M. O. Ogunbunmi and S. Bobev, *Inorg. Chem.*, 2021, **60**, 14426–14435.

[107] K. Kersten, R. Kaur and A. Matzger, *IUCrJ*, 2018, **5**, 124–129.

[108] C. Ge, J. Liu, X. Ye, Q. Han, L. Zhang, S. Cui, Q. Guo, G. Liu, Y. Liu and X. Tao, *J. Phys. Chem. C Nanomater. Interfaces*, 2018, **122**, 15744–15752.

[109] A. Polman, M. Knight, E. C. Garnett, B. Ehrler and W. C. Sinke, *Science*, 2016, **352**, aad4424.

[110] O. Almora, D. Baran, G. C. Bazan, C. Berger, C. I. Cabrera, K. R. Catchpole, S. Erten-Ela, F. Guo, J. Hauch, A. W. Y. Ho-Baillie, T. J. Jacobsson, R. A. J. Janssen, T. Kirchartz, N. Kopidakis, Y. Li, M. A. Loi, R. R. Lunt, X. Mathew, M. D. McGehee, J. Min, D. B. Mitzi, M. K. Nazeeruddin, J. Nelson, A. F. Nogueira, U. W. Paetzold, N.-G. Park, B. P. Rand, U. Rau, H. J. Snaith, E. Unger, L. Vaillant-Roca, H.-L. Yip and C. J. Brabec, *Adv. Energy Mater.*, 2021, **11**, 2102526.

[111] M. Saifullah, J. Gwak and J. H. Yun, *J. Mater. Chem. A Mater. Energy Sustain.*, 2016, **4**, 8512–8540.

[112] B. Weng, M.-Y. Qi, C. Han, Z.-R. Tang and Y.-J. Xu, *ACS Catal.*, 2019, **9**, 4642–4687.

[113] X. Ning and G. Lu, *Nanoscale*, 2020, **12**, 1213–1223.

[114] K. Bu, X. Zhang, J. Huang, M. Luo, C. Zheng, R. Wang, D. Wang, J. He, W. Zhao, X. Che and F. Huang, *Chem. Commun. (Camb.)*, 2019, **55**, 4809–4812.

[115] G. Zhang, B. Zhang, H. Chen, X. Zhang, C. Zheng, J. Lin and F. Huang, *J. Alloys Compd.*, 2014, **591**, 6–10.

[116] X. Huang, S.-H. Yang, W. Liu and S.-P. Guo, *Inorg. Chem.*, 2022, **61**, 12954–12958.

[117] Y. Xiao, S.-H. Zhou, R. Yu, Y. Shen, Z. Ma, H. Lin and Y. Liu, *Inorg. Chem.*, 2021, **60**, 9263–9267.

[118] Y. Chi, T.-F. Jiang, H.-G. Xue and S.-P. Guo, *Inorg. Chem.*, 2019, **58**, 3574–3577.

[119] Q.-N. Yan, B.-W. Liu, X.-M. Jiang, J.-X. Zhao, S.-M. Pei, W.-F. Chen and G.-C. Guo, *Dalton Trans.*, 2022, **51**, 5561–5566.

[120] X. Zhang, J. He, R. Wang, K. Bu, J. Li, C. Zheng, J. Lin and F. Huang, *Sol. RRL*, 2018, **2**, 1800021.

[121] C. Liu, P. Hou, W. Chai, J. Tian, X. Zheng, Y. Shen, M. Zhi, C. Zhou and Y. Liu, *J. Alloys Compd.*, 2016, **679**, 420–425.

[122] Y. Liu, D. Xuan, Z. Song, L. Geng, B. Zhang and T. Liu, *J. Solid State Chem.*, 2022, **315**, 123457.

[123] C. Liu, Y. Xiao, H. Wang, W. Chai, X. Liu, D. Yan, H. Lin and Y. Liu, *Inorg. Chem.*, 2020, **59**, 1577–1581.

[124] H. Li, C. D. Malliakas, F. Han, D. Y. Chung and M. G. Kanatzidis, *Chem. Mater.*, 2015, **27**, 5417–5424.

[125] A. Qiao, H. Tao and Y. Yue, *J. Non Cryst. Solids*, 2019, **521**, 119476.